Electrical Power and Energy Systems 157 (2024) 109862

Contents lists available at ScienceDirect

International Journal of Electrical Power and Energy Systems

journal homepage: www.elsevier.com/locate/ijepes

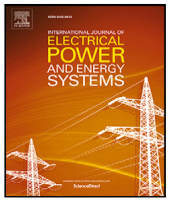

A grid forming controller with integrated state of charge management for V2G chargers

Ander Ordono [a,*], Francisco Javier Asensio [a], Jose Antonio Cortajarena [b], Inmaculada Zamora [c], Mikel González-Pérez [a], Gaizka Saldaña [c]

[a] Department of Electrical Engineering, University of the Basque Country (UPV/EHU), Avd. Otaola, 29, Eibar, 20600, Spain
[b] Department of Electronic Technology Engineering, University of the Basque Country (UPV/EHU), Avd. Otaola, 29, Eibar, 20600, Spain
[c] Department of Electrical Engineering, University of the Basque Country (UPV/EHU), Alameda Urquijo, s/n, Bilbao, 48013, Spain

ARTICLE INFO

Keywords:
Electric vehicle
Frequency regulation
Grid forming
V2G

ABSTRACT

Vehicle-to-grid (V2G) technology offers an innovative solution to provide grid services using electric vehicle (EV) batteries. This work proposes a novel grid forming (GFM) controller for V2G applications which can ensure the voltage source behaviour and provide support to the grid, regardless of the state of charge (SoC) and the charging requirements of the battery. This is achieved by integrating a SoC controller that modifies the classical GFM algorithm. The controller only relies on the SoC and power measurements, achieving a decentralized without the need of communication. With the proposed approach, the V2G charger will always behave as a voltage source that provides inertial response and voltage support to the grid. The primary frequency regulation, on the other hand, will depend on the battery status and charging needs. Frequency regulation could be enabled, disabled or it could be limited to some perturbations (under/over frequencies). Moreover, the SoC controller provides freedom to tune the frequency support of the device, limiting it to inertial response or extending its contribution along the time. The tuning of the system parameters is addressed in detail to ensure a damped response under all the operation scenarios provided by the SoC controller. Its performance and stability is evaluated using small signal transfer functions. Finally, it is validated both in simulation and experimentally.

1. Introduction

In the recent years, power grids are integrating increasing amounts of non-dispatchable renewable energy sources (RES), shifting towards a more environmentally friendly grid. However, new challenges arise due to the paradigm shift [1]. On the one hand, the grid management complexity increases due to the stochastic behaviour and the reduced power reserves of RES [2]. On the other hand, as the kinetic energy stored in rotating masses of conventional plants (inertia) is replaced by inverter-based RES, the grid turns weaker and prone to bigger and faster voltage and frequency excursions [3]. All in all, the grid paradigm shift leads to a more dynamic and complex grid power management [4].

In this scenario, grid operators are implementing strategies to ensure grid stability and reliability. Energy Storage Systems (ESS), demand management and RES curtailment are among the most relevant approaches to provide flexibility [5]. Related to ESS, Vehicle-to-Grid (V2G) has also arisen as a promising solution [6]. V2G chargers enable bidirectional energy flow between electric vehicles (EVs) and the grid, allowing them to not only consume, but also provide energy back to the grid when needed. By aggregating multiple EV batteries, a significant amount of flexibility can be provided to the grid, removing the need of ESS systems and reducing the investment costs [7].

Several services have been proposed for V2G applications [8], being the most interesting those which require fast response and have a low battery degradation impact (low energy, high power). In this context, the contribution of EVs to the Load Frequency Control has been extensively studied [9]. Several work have shown that V2G systems can contribute to keep the frequency close to its rated value while ensuring a proper SoC management of the EVs [10–12]. However, these controllers usually rely on a communication link to a centralized controller, increasing the complexity when the number of chargers is high or they are geographically dispersed. To prevent this issue, services which can be provided based on local measurements have gained attention for V2G applications (distributed approach). Supporting the grid through inertia emulation, primary frequency regulation and voltage support stand out.

* Corresponding author.
E-mail address: ander.ordono@ehu.eus (A. Ordono).

https://doi.org/10.1016/j.ijepes.2024.109862
Received 18 September 2023; Received in revised form 15 January 2024; Accepted 8 February 2024
Available online 10 February 2024

As other inverter-based resources, V2G chargers could support the grid using two control strategies: grid following (GFL) and grid forming (GFM) [13]. GFL is the most mature and widespread strategy for these applications. A synchronization mechanism, usually a Phase-Locked Loop (PLL), is used to detect the grid phase. Based on this information, the exchanged current amplitude and phase is regulated to handle the active and reactive power transfer. From grid perspective, the power converter behaves as a controlled current source. GFL-based V2G chargers have been extensively studied in literature, where the main goal is to maximize the grid support while ensuring a proper SoC management. Authors in [14] have proposed a control strategy in which the charger could operate in 3 discrete states (charge, discharge or idle) depending on local measurements. To provide a smoother support, the smart charging concept has also been proposed by several authors [15–17]. In these, the charger power setpoint is modified through a droop controller. Smart charging strategies require the charger to operate far below the rated power to provide up and down regulation, which has a negative impact on the efficiency of the power electronics. To provide a symmetrical support and optimize the charging efficiency of the system, [18] divides the EV charger operation into two regions: the frequency support region and the forced-charge boundary region. Even if the EV is charged efficiently, the frequency regulation capability is lost during the forced-charge boundary. Adaptive droops, in which the droop coefficient is modified using the state of charge (SoC) of the vehicle have also been proved useful to provide keep the SoC limited to a certain range or to prevent an excessive battery degradation. Different relations between the droop coefficient and the SoC have been proposed in literature, depending on the goal [15,19]. Finally, V2G chargers operating as GFL have also been proposed to provide some synthetic inertia. This is usually achieved by adding a derivative term to the droop controller [20,21]. [22] have merged the inertial response and the adaptive droop concept together in a hybrid system based on a EV battery an ultra-capacitors.

Despite the popularity of GFL strategies in V2G chargers, they face some limitations: they do not operate properly on weak grids nor can provide without an existing grid (standalone). [23]. In this scenario, GFM strategies have emerged as an alternative to face the issues related to GFL and achieve a 100% IBR-based grid [24]. Despite sharing the same hardware, GFM devices behave as controlled voltage sources which can mimic the behaviour of synchronous generators (SGs), providing accurate inertia, higher stability under weak grids and standalone operation. V2G chargers operating as GFM devices could be interesting for small scale grid applications or to ensure the power supply under blackouts. Authors in [25] have proposed a community of EVs operating as Virtual Synchronous Generators (VSG) that ensures the supply in case of power failure. VSGs for low power single-phase EV chargers have also been proposed in [26,27]. The former reference is focused on the dynamic response to grid perturbations, whereas the latter aims to optimize the charger performance with a reduced DC link capacitance. Authors in [28] have also suggested a V2G charger based on a GFM droop controller, focusing on active/reactive power decoupling without inertia emulation.

In all the previous GFM strategies, the SoC limits and the charging requirements of the EV were not considered. In fact, the GFM operation considering the EV battery has not been studied in depth in literature. A SoC management was described in [29], but the response of the controller and its stability under the different scenarios was not addressed in detail. Limiting the contribution to inertial response has also been suggested as a solution to prevent SoC drifts for chargers [30,31]. However, this approach might lead to underusage of the battery, as there are scenarios in which the primary frequency regulation of EVs could be advantageous both for the EV and the grid.

Considering all the mentioned above, this paper aims to develop a GFM controller with an integrated SoC management for V2G charger applications. When the battery SoC is inside its operational limits and no charging is required, the V2G charger will behave as a conventional GFM device, providing inertia emulation, primary frequency and voltage support. However, when the SoC limits are hit or charging is required, the SoC controller will reduce the primary frequency support depending on the perturbation type, limiting its contribution to meet the SoC requirements. The SoC controller provides freedom to tune the transient support of the device, limiting it to inertial response or providing time-extended contributions. The impact of the SoC controller on the stability and response of the V2G is addressed in detail, and parameters are tuned to provide a damped response. The proposed controller will only use the SoC and power measurements to operate, achieving a decentralized approach and not needing frequency measurements.

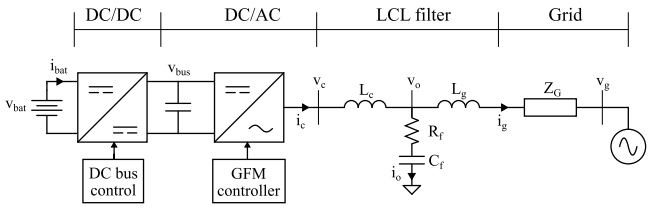

Fig. 1. One-line diagram of a 3-phase EV charger using a GFM strategy.

This paper is organized as follows. Section 2 describes the overall structure of the V2G charger, focusing on the inverter side and its interaction with the AC grid. The GFM strategy, the internal control loops and the SoC controller are described in detail, including the identified operating modes, which depend on the SoC conditions and charging requirements. Section 3 evaluates the transfer function of the system for the previously identified operating modes. The performance of the V2G charger can be evaluated by considering two scenarios, which depend on the status (enabled/disabled) of the SoC controller. The controller is tuned to prioritize the damping of the response. The performance of the proposed control strategy under different operating modes is validated in Section 4, both using a simulation and an experimental setup. Finally, the main conclusions are gathered in Section 5.

2. System description

Fig. 1 shows the simplified diagram of a 3-phase bidirectional EV charger. The EV charger is composed of a DC/DC and a DC/AC stage, connected through an intermediate DC bus (v_{bus}). The DC/AC stage is connected to the grid using a LCL filter, which is designed to meet the harmonic distortion requirements of the grid [32]. The filter is composed of an inverter-side inductor L_c, a grid-side inductor L_g and a capacitor C_f. A damping resistor R_f can be connected in series to the capacitor to attenuate the resonance peak of the filter. The grid is represented using its equivalent Thévenin circuit, composed of a voltage source v_g and its equivalent series impedance Z_G. The grid impedance includes inductive L_G and resistive R_G components.

When EV chargers operate in GFL mode, the DC/AC regulates the intermediate voltage v_{bus} and the reactive power (or power factor) exchanged with the grid, whereas the DC/DC manages the active power which is exchanged with the battery. In GFM, the control structure is modified: the DC/DC is used to regulate v_{bus}, whereas the DC/AC manages the active and reactive power exchanged with the grid. For the sake of simplicity, this analysis will only focus on the GFM strategy of the DC/AC stage. The dynamics of the DC/DC stage are neglected, considering a stiff DC voltage source.

2.1. GFM control structure

The GFM control of the DC/AC stage of the V2G charger is shown in Fig. 2. The controller is implemented using the synchronous dq frame. All the parameters and equations in the diagram are based on the per unit system (pu), except for the base angular frequency ω_b and the internal angular position θ_r, which are given in rad/s and rad respectively. The GFM is composed of 4 main blocks:

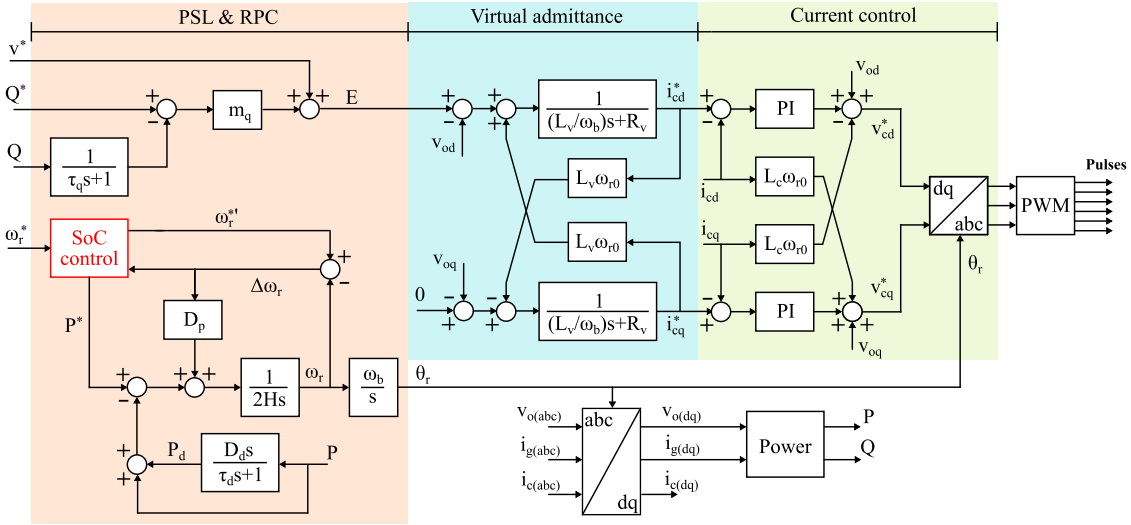

Fig. 2. Grid forming strategy for the DC/AC stage of the V2G charger.

- Power Synchronization Loop (PSL)
- Reactive Power Control (RPC)
- Virtual Admittance
- Current Controller

A brief description of each control block is given in the following subsections. The proposed SoC controller, marked in red in the figure, will be described more into detail in Section 2.2.

2.1.1. Power synchronization loop

The PSL generates the angular frequency ω_r and position θ_r of the output voltage of the GFM system. θ_r is used to convert variables to and from dq system, as shown in Fig. 2. Compared to GFL inverters, which synchronize to the existing grid using grid voltage measurements and a PLL, the GFM inverters use an active power based synchronization. This allows them to operate in standalone conditions, without an existing grid. The proposed PSL is based on a VSG algorithm, which emulates the swing equation of SGs [33]:

$$\frac{d\omega_r}{dt} = \frac{1}{2H}(P^* - P + D_p(\omega_r^{*\prime} - \omega_r) - P_d) \tag{1}$$

In the previous equation, P^* is the active power command, P is the measured active power, ω_r is the output angular frequency of the controller, D_p is the static damping term and H is the virtual inertia term. The term $\omega_r^{*\prime}$ is the angular frequency command, which can be modified by the SoC control algorithm.

H is selected to provide dynamic frequency support to the grid. For this analysis, an inertia of 8 s is used. D_p, which is the inverse of the droop coefficient, determines the steady-state active power value under grid frequency deviations (primary frequency regulation). The typical values of D_p ranges between 20 to 50 pu, to ensure a proper power sharing among the sources connected to the grid. For this analysis, a D_p of 50 pu is selected. This means that a change in the grid frequency of 0.02 pu will lead to a change of 1 pu in the active power of the system.

As H and D_p terms are usually defined by the system operator, the active power loop dynamics are fixed [34]. The dynamic damping power term, P_d, is added to the swing equation to improve the transient response of the active power loop. The dynamic damping term will not affect the steady-state response of the swing equation, so it is useful to decouple the transient and steady-state response. Among existing dynamic damping strategies, a power derivative term (2) is proposed, where D_d is the dynamic damping coefficient. The value of the dynamic damping term D_d will be tuned in Section 3 [35].

$$P_d = \frac{D_d s}{\tau_d s + 1} \tag{2}$$

The dynamic damping term includes a low pass filter (LPF) with a time constant τ_d. The bandwith of this filter is set to 20 Hz. This will provide damping in the range of the active power loop (1–3 Hz), but it will prevent the interactions with synchronous oscillations (50 Hz) that could make the system unstable [36].

2.1.2. Reactive power control

The RPC generates the voltage setpoint E of the GFM, emulating the reactive power droop behaviour of SGs according to:

$$E = v^* + m_q\left(Q^* - \frac{Q}{\tau_q s + 1}\right) \tag{3}$$

Where v^* and Q^* are the voltage and reactive power commands, m_q is the reactive power droop, and Q is the measured reactive power. A first order low-pass filter (LPF) with a time constant τ_q is used to remove high frequency components and to adjust the dynamics of the reactive power loop. The reactive power droop is set to a typical value of 0.1 pu. The filter time constant is set to 20 ms.

2.1.3. Virtual admittance

The virtual admittance algorithm emulates an impedance between the RPC voltage setpoint E and the measured capacitor voltage v_o. The virtual admittance behaviour is equivalent to a voltage controller with a virtual impedance, but with the advantage of removing the voltage controller. The virtual impedance is useful for connecting GFM inverters to strong grids, in which the line impedance is small compared to the rated power of the converter, which could be the case of a V2G charger. By increasing the inductive term of the virtual impedance, the active and reactive power can be decoupled regardless of the grid impedance, allowing a proper operation of the PSL and RPC controllers. Additionally, the virtual impedance can reduce the active and reactive power loop dynamics, improving the stability of the system [37].

The following equation describes the implementation of the virtual admittance strategy in the dq frame:

$$\frac{di^*_{cdq}}{dt} = \frac{\omega_b}{L_v}\left(E - v_{odq} - R_v i^*_{cdq} + j\omega_{r0} L_v i^*_{cdq}\right) \tag{4}$$

Where i^*_{cdq} is the converter current vector setpoint, v_{odq} is the capacitor voltage vector feedback, and R_v and L_v are the virtual resistance and inductance values. By considering that the angular frequency variation of the GFM converter will be small, the angular frequency ω_{r0} in the coupling terms can be considered constant and equal to 1 pu.

The proposed algorithm uses a virtual inductance and resistance of 0.3 and 0.06 pu, respectively. The addition of a virtual impedance is used to damp the synchronous oscillations, which are out of the scope of this analysis [38].

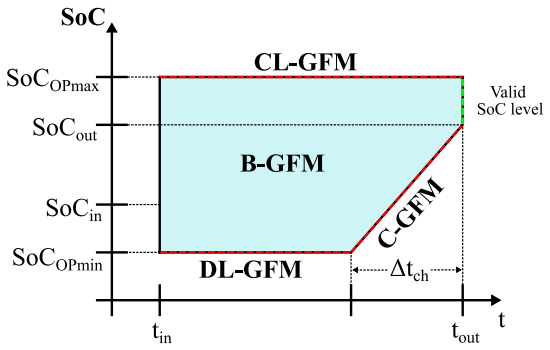

Fig. 3. Grid forming operation modes based on SoC level and charging time.

2.1.4. Current controller

The converter current is regulated using a PI controller. To improve the system response, it includes dq decoupling terms and capacitor voltage feedforward:

$$v^*_{cdq} = (i^*_{cdq} - i_{cdq})(k_p + k_{ic}/s) + j\omega_{r0}L_c i_{cdq} + v_{odq} \quad (5)$$

v^*_{cdq} is the converter voltage vector setpoint, i_{cdq} is the converter current vector feedback, k_{pc} is the proportional gain and k_{ic} is the integral gain. As in the virtual admittance, the term ω_{r0} in the decoupling terms can be considered constant. A modulus optimum tuning approach is used to select the PI gains [39].

The current controller bandwidth is set 20 times lower than the switching frequency of the converter (f_{sw}), which is 10 kHz. The 500 Hz bandwidth is high enough compared to the bandwidth of the PSL and RPC loops, and hence, it dynamics can be neglected in the analysis.

2.2. SoC controller

V2G chargers, due to their bidirectional capability, could operate as GFM devices. However, the SoC of the battery must be properly managed during operation. The GFM controller should meet the following conditions:

- The battery SoC must be limited to an operational range to prevent battery degradation. The lower and upper operational limits are defined as SoC_{OPmin} and SoC_{OPmax}, which are more restrictive that the absolute battery limits SoC_{min} and SoC_{max}.
- When the EV is unplugged, it should have enough charge to meet the mobility requirements of the EV user.

2.2.1. GFM modes under SoC control

Fig. 3 shows a SoC vs time diagram of a plugged EV. The vehicle is plugged into the V2G charger at time t_{in}, with an initial charge level SoC_{in} (%). The owner of the vehicle will unplug the vehicle from the charging station at time t_{out}, expecting a charge level of at least SoC_{out} (%). It is assumed that the plug out-time and expected charge are introduced by the user or they can be estimated using historical data. Moreover, the required charge will always be lower than SoC_{OPmax}. According to the figure, 4 operation modes can be identified: The B-GFM, in which the EV charger operates as a conventional GFM device. The CL-GFM and DL-GFM, in which transient frequency support is provided, but the primary frequency support is limited to prevent crossing the operational limits. Finally, the C-GFM, in which the priority is to meet the charge level of the EV and hence, only transient support is provided. A more detailed explanation of each mode is given in Table 1. In all the cases, the voltage support is always available, as it depends on reactive power.

It should be noted that even if the controllable voltage source behaviour is kept in all the operating modes, the standalone operation capability is only available in B-GFMI mode. In the remaining modes, the EV charger will contribute to the stability of the grid by providing transient frequency support, but the steady state contribution or primary frequency support, which depends on the static damping power is not guaranteed. The system should rely on other GFL or GFM devices to ensure the stable operation. An additional emergency mode could also be developed, in which the SoC controller could be deactivated when the grid frequency goes below or above a threshold to prioritize the grid stability over the battery conditions. This analysis is out of the scope of this work.

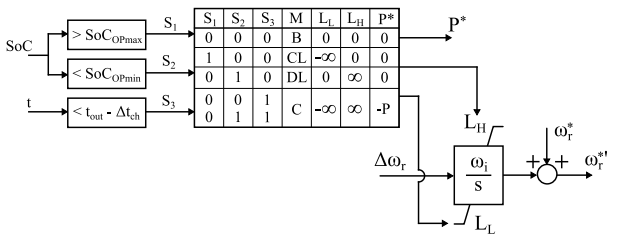

Fig. 4. Implementation of SoC controller, including logic table.

2.2.2. Controller implementation

The proposed SoC controller implementation is shown in Fig. 4. It is based on an integral action, which will remove the frequency deviation error ($\omega^*_r - \omega_r$), ensuring that the power setpoint P^* is met regardless of the grid conditions. A dynamic saturation is used to handle the contribution to under and over-frequencies independently. Additionally, it can be used to disable the SoC controller by setting the saturation levels to 0.

A logic table is used to obtain the integrator upper and lower dynamic limit, L_H and L_L, and the charging setpoint P^*. The logic table uses three boolean inputs (S_1, S_2, S_3) to determine if the SoC is inside the operational limits and to check if charging is required. These boolean inputs are the ones defined in the conditions column of Table 1. A hysteresis could be added to prevent continuous triggering of boolean inputs S_1 and S_2, but it is neglected for the sake of simplicity. The "M" column in Fig. 4 identifies the operation mode defined in Table 1.

3. Transfer function & stability analysis

The proposed controller has a non-linear behaviour due to the saturation block introduced by the SoC controller. However, its performance can be evaluated considering two independent scenarios:

1. SoC controller disabled: The integral action can be neglected from the study. This controller is disabled in the following modes:
   - B-GFM
   - DL-GFM under over-frequencies
   - CL-GFM under under-frequencies
2. SoC controller enabled: The integral action modifies the angular frequency command of the GFM algorithm. The SoC controller is enabled in the following modes:
   - C-GFM
   - DL-GFM under under-frequencies
   - CL-GFM under over-frequencies

The linearized model of the active power loop is shown in Fig. 5. The term Δ is added to all the signals to indicate that they are small signal variations. The SoC controller branch is marked in red, and it must be considered only when the SoC controller is active. The impact

Table 1
Operation modes description.

Mode	Description	Condition
B-GFM	Basic operation. The SoC control does not modify ω_r^*. The system operates as a conventional grid forming device. The charger provides inertia emulation and primary frequency regulation capability.	$SoC \in (SoC_{OPmin}, SoC_{OPmax})$
DL-GFM	Discharge-limited operation. It prevents an excessive discharge of the battery by limiting active power support to grid under-frequencies. The charger provides transient frequency support, and primary frequency regulation under over-frequencies.	$SoC \leq SoC_{OPmin}$
CL-GFM	Charge-limited operation. It prevents an excessive charge of the battery by limiting the active power support to grid over-frequencies. The charger provides transient frequency support, and primary frequency regulation under under-frequencies.	$SoC \geq SoC_{OPmax}$
C-GFM	Charging operation. It ensures that EV charge level is met before plug-out time. During this time, the active power support to both under and over-frequencies is limited. The charger only provides transient frequency support. This mode is activated when the remaining plug out time $(t_{out} - t)$ is equal or lower than the charging time Δt_{ch}. Time is given in hours. C_{ev} is the battery capacity in kWh and P^* is the charging power in kW. P^* should be smaller than charger maximum power to prevent overloading condition	$t_{out} - t \leq \Delta t_{ch}$ $\Delta t_{ch} = \frac{C_{EV}}{100} \frac{SoC_{out} - SoC}{\lvert P^* \rvert}$

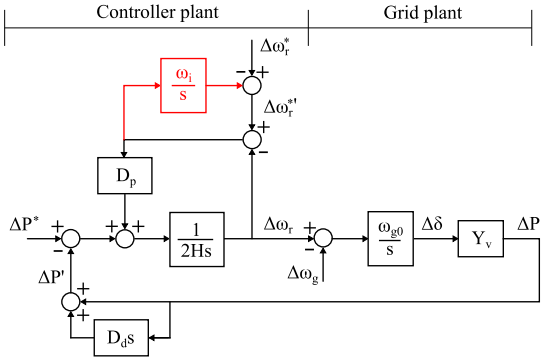

Fig. 5. Small-signal model of the active power loop.

of the voltage and the reactive power are neglected, considering an inductive line that provides proper decoupling of active/reactive powers. For convenience, the LPF of the dynamic damping, determined by τ_d, is also neglected. This simplification is valid for analysing frequency components that are well below the bandwidth of the filter, which is the case of the PSL loop. The term $\Delta\omega_g$ is the grid angular frequency variation, which is considered as an external perturbation for the plant. ω_{g0} is the angular frequency value at the linearization point, in rad/s.

The simplified model of the grid plant is obtained from the active power transfer equation on inductive lines (6), where δ is the phase shift between the GFM and the grid voltage, in rad/s. The virtual reactance ($X_v = L_v$ in pu) is considered much higher than the grid impedance, so that the latter can be neglected in the analysis. This would be the case of an EV charger connected to a utility grid or microgrid, in which the overall power of the charger is small compared to the rated power of the system.

$$P = \frac{EV_g}{X_v} \sin\delta \tag{6}$$

The previous equation can be linearized around the operating angle δ_0. Assuming that the voltages are close to the base values, and that the operating angle is small, the relation between the active power and the angle is inversely proportional to the virtual reactance, or proportional to the virtual susceptance Y_v:

$$\frac{dP}{d\delta} = \frac{EV_g \cos\delta_0}{2\pi L_v}\delta \approx \frac{1}{X_v} = Y_v \tag{7}$$

Table 2 provides an overview of the active power open-loop $\Delta P/(\Delta P^* - \Delta P)$ and closed-loop $\Delta P/\Delta P^*$ transfer functions, taking into account the SoC controller state. The response to grid frequency perturbations $\Delta P/\Delta\omega_g$ is also included.

Table 2
Active power transfer functions with and without SoC controller.

	SoC control enabled	SoC control disabled
$\frac{\Delta P}{\Delta P^* - \Delta P}$	$\frac{Y_v\omega_{g0}(D_d s+1)(s+\omega_i)}{2Hs^3+(2H\omega_i+D)s^2}$	$\frac{Y_v\omega_{g0}(D_d s+1)}{2Hs^2+Ds}$
$\frac{\Delta P}{\Delta P^*}$	$\frac{Y_v\omega_{g0}(s+\omega_i)}{2Hs^3+(D_p+2H\omega_i+Y_v\omega_{g0}D_d)s^2+Y_v\omega_{g0}(1+D_d\omega_i)s+Y_v\omega_{g0}\omega_i}$	$\frac{Y_v\omega_{g0}}{2Hs^2+(D_p+Y_v\omega_{g0}D_d)s+Y_v\omega_{g0}}$
$\frac{\Delta P}{\Delta\omega_g}$	$-\frac{Y_v\omega_{g0}(2Hs^2+(2H\omega_i+D_p)s)}{2Hs^3+(D_p+2H\omega_i+D_dY_v\omega_{g0})s^2+Y_v\omega_{g0}(1+D_d\omega_i)s+Y_v\omega_{g0}\omega_i}$	$-\frac{Y_v\omega_{g0}(2Hs+D_p)}{2Hs^2+(D_p+Y_v\omega_{g0}D_d)s+Y_v\omega_{g0}}$

3.1. SoC control disabled

When the SoC controller is not enabled, the active power loop behaves as a second order system. According to the closed loop equation in Table 2, the bandwidth of the active power response, ω_c, depends on the inertia and virtual susceptance (8), whereas the damping ξ also depends on the D_p and D_d terms (9). The term D_d does not affect the steady state response under frequency perturbations, only depending on D_p. This can be clearly seen by applying the final theorem to the closed loop equation.

$$\omega_c = \sqrt{\frac{Y_v\omega_{g0}}{2H}} \tag{8}$$

$$\xi = \frac{1}{2\omega_c}\frac{D_p + Y_v\omega_{g0}D_d}{2H} \tag{9}$$

The impact of the dynamic damping D_d on the closed loop response of the active power loop is shown in Fig. 6(a), whereas the response against grid frequency perturbations is shown in Fig. 6(b). The closed loop response provides a proper power control for frequencies up to 1.2–2 Hz, consistent with expected bandwidth. Increasing D_d allows the attenuation of the resonance peak in the transfer function, albeit with a slight reduction in bandwidth. When $D_d = 0$, the damping of the system is lower than 0.3. By setting $D_d = 0.13$ pu, the system is critically overdamped. The $\Delta P/\Delta\omega_g$ transfer function provides a DC gain of 34 dB, regardless of the dynamic damping term. This gain matches the static damping term D_p.

The impact of the dynamic damping can also be assessed by analysing the evolution of the poles, as depicted in Fig. 7. In this figure, the real part of the pole σ is represented in the x-axis and the imaginary part ω is depicted in the y-axis. As the D_d term increases, the poles associated with the electromechanical equation move towards the left half-plane, which enhancing the system damping. Lines representing different ξ values have been added to the graph. The term D_d could be selected using different approaches. One method is to find a suitable compromise between speed response and overshoot by setting $\xi = 1/\sqrt{2}$. This corresponds to a D_d value of 0.1 pu.

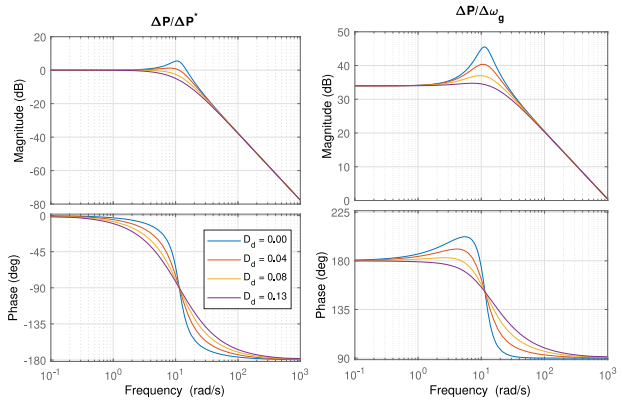

(a) Closed loop response (b) Frequency perturbation response

Fig. 6. System response when SoC controller is disabled.

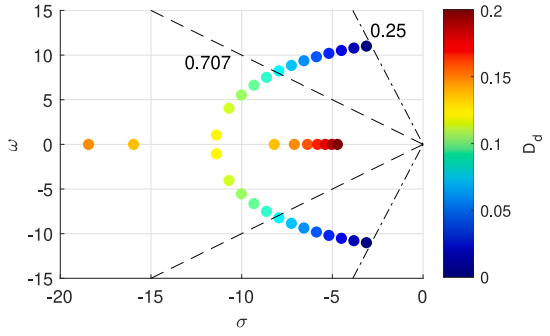

Fig. 7. CL pole evolution under a D_d sweep. SoC control disabled.

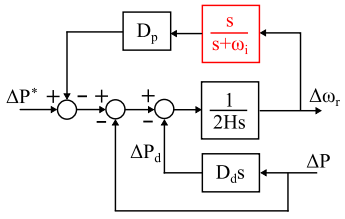

Fig. 8. Small-signal model of the PSL.

3.2. SoC control enabled

When the SoC control is enabled, the integral action of the SoC controller modifies the static damping term D_p, adding a first order high-pass filter (HPF) in series. In this scenario, the relation between the angular frequency deviation $\Delta\omega_r$ and the active power ΔP can be rewritten as (10). The integral gain ω_i, in rad/s, determines the bandwidth of the filter. The simplified small-signal diagram of the PSL is shown in Fig. 8, where the red block represents the HPF introduced by the SoC control. Hence, the main effect of the SoC controller is to remove the contribution of the static damping power, which is equivalent to the primary frequency regulation. The higher the bandwith of the filter, the faster the static damping power will be removed.

$$\frac{\Delta P}{\Delta\omega_r} = D_p \frac{s}{s+\omega_i} \tag{10}$$

When the SoC controller is enabled, the dynamic damping term plays a key role in the stability of the system, specially when the integral gain is high. Under these conditions, the contribution of D_p can be nearly neglected, with damping primarily provided by D_d term.

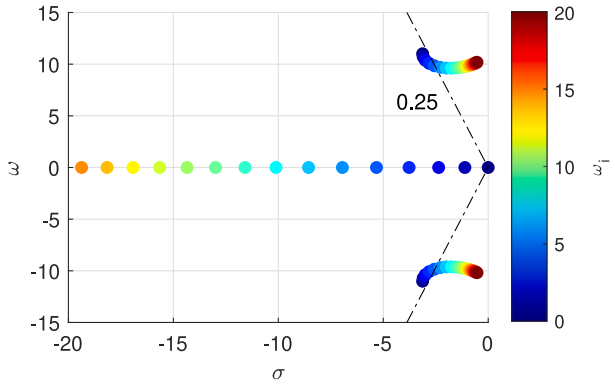

Fig. 9. CL pole evolution under a ω_i sweep, without dynamic damping.

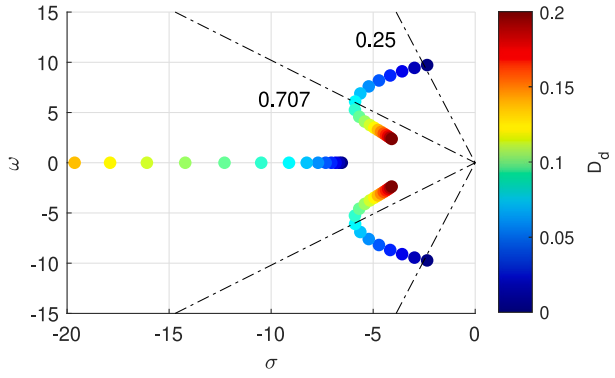

Fig. 10. CL pole evolution under a D_d sweep, with $\omega_i = 5$ rad/s.

The influence of ω_i on the stability of the system becomes evident when analysing the pole displacement under a ω_i sweep with a null dynamic damping term (Fig. 9). As the integral gain is increased, the poles associated with the mechanical system progressively shift toward the right-hand plane, resulting in a reduction of damping and a potential loss of stability in the system.

For this analysis, a $\omega_i = 5$ rad/s is proposed. With this bandwidth, the static damping effect will be removed in around 0.8 s (4 time constants). The pole displacement under a D_d sweep is given in Fig. 10. For a certain integral gain, increasing D_d will increase the damping of the electromechanical poles of the system, as observed in the previous analysis. However, the damping increase is considerably reduced when going above a certain critical D_d value. Beyond this value, the impact on the damping of the electromechanical mode is considerably reduced, and instead, the angular frequency decreases. As the target of this controller is to provide a damped response, a $D_d = 0.08$ pu is used for simulation and experimental tests. This is the value in which the damping of the electromechanical poles changes its trend, identified graphically in Fig. 10.

The bode responses of the system with the SoC controller enabled and disabled are compared in Fig. 11. The closed loop active power response remains nearly equal, indicating that the SoC controller does not impact its performance. However, the response of the system under grid frequency perturbations is altered when the SoC controller is enabled. With the SoC controller enabled, the system exhibits zero gain at DC value, indicating that the active power will return to the desired setpoint after a perturbation. The magnitude of the low frequency components can be modified by varying the integral gain of the SoC controller, ω_i.

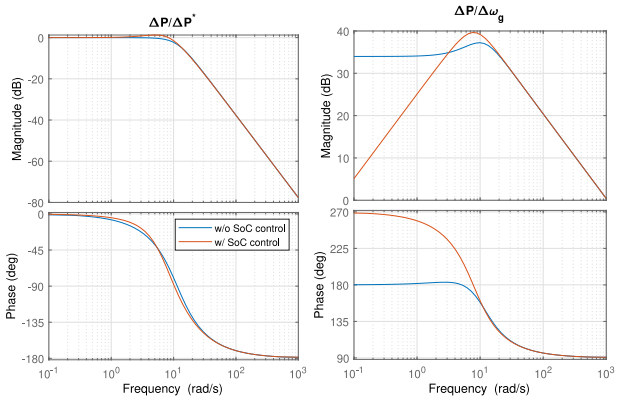

(a) Closed loop response (b) Frequency perturbation response

Fig. 11. Bode response when SoC controller is enabled and disabled.

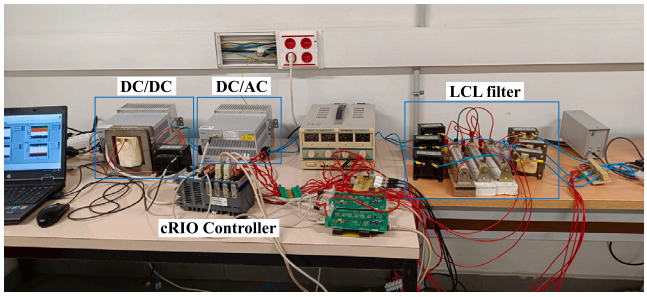

Fig. 12. Experimental setup.

4. Simulation & experimental validation

The performance of the proposed controller has been tested both in simulation and experimentally. The parameters which have been used for validating the system are summed up in Table A.3.

For the simulation, a Simulink model based on Fig. 1 has been developed. The grid is modelled using its Thévenin equivalent circuit. The impact of the DC/DC stage is neglected by considering a stiff DC voltage source, and an average DC/AC model is used to remove switching frequency effects. These assumptions have been extensively used in literature when modelling grid-connected GFM devices [40,41].

The experimental setup and its main components are shown in Fig. 12. The DC/DC and DC/AC stages are based on INF-50 power inverters from Dutt Electronics. The bidirectional DC/DC is built using two of the inverter's half bridges, operating as an interleaved buck/boost. The battery is emulated using a BIC-2200-96 from Mean-well, which provides a 96 Vdc bidirectional supply. For the 3-phase grid, a Pacific Power 320-AMX supply is used. Off-the-shelf components have been used for passive and sensoring devices. The control algorithm is implemented in a cRIO-9040, which includes a Kintex-7 70T FPGA and a Dual-Core 1.30 GHz CPU. The cRIO device includes an acquisition task that captures analog inputs and controller internal signals at 10 kHz. All the analog inputs include a 3.3 kHz antialiasing filter.

4.1. Response to active power setpoint step

The theoretical analysis from Section 3 concluded that the active power closed loop dynamics were highly dependent on H, D_p and D_d. As the first two parameters are usually defined by the system operator or grid requirements, D_d can be used to manage the ξ of the active power response.

Fig. 13 shows the effect of the dynamic damping term D_d on the active power closed loop response. The figure presents both the experimental and simulated responses of the GFM under a power setpoint step of −0.1 pu, using D_d values of 0 and 0.1 pu. Both experimental and simulation results are overlapped, showing identical power dynamics. The measured active power includes some ripple due to the switching noise of the real power converter, which does not appear in the simulated averaged model. The bandwidth of the active power controller is nearly constant, around 1.8 Hz. When D_d is set to 0, the active power response has a $\xi = 0.27$. However, when it is set to 0.1 pu, the damping is considerably increased to $\xi = 0.85$.

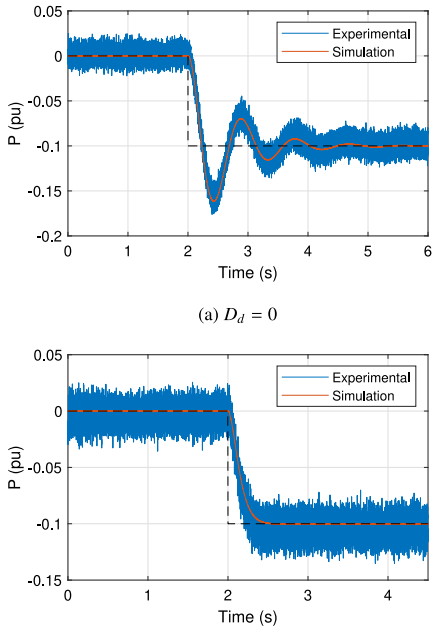

(a) $D_d = 0$

(b) $D_d = 0.1$

Fig. 13. Active power under a power setpoint of −0.1 pu using different D_d.

The active power closed loop response is barely modified when the SoC controller is enabled and the integral action is executed (see Fig. 11(a)) Hence, the previous analysis is valid for all the operation modes defined in Table 1.

4.2. Response to frequency perturbations

The operation mode of the EV charger will determine the response of the system to frequency perturbations. Simulation and experimental results are carried out for B-GFM, CL-GFM and C-GFM modes. For the sake of simplicity, DL-GFM mode is not included because its behaviour is symmetrical to the CL-GFM mode. The results, which will be discussed more into detail in the next subsections, are plotted in Fig. 14. The figure includes the angular frequency of the grid, the angular frequency of the GFM and both measured active and reactive powers. Experimental and simulation results are superimposed, showing similar results.

For all the operation modes, the testing sequence is the same. The grid starts at the rated frequency of 1 pu. A first over-frequency event is generated by increasing the grid frequency to 1.002 pu using a step. After some time, the grid frequency experiences a frequency variation of −0.004 pu, finishing in a steady state value of 0.998 pu. By transitioning from an over-frequency to an under-frequency scenario, the non-linear behaviour of the CL-GFM mode can be identified.

The analysis in the following subsections will be mainly focused on the active power response, as the proposed algorithm does not modify the performance of the RPC. As it is expected in GFM converters, there is a coupling between the exchanged active and reactive power. The frequency steps slightly modify the reactive power due to the resistive

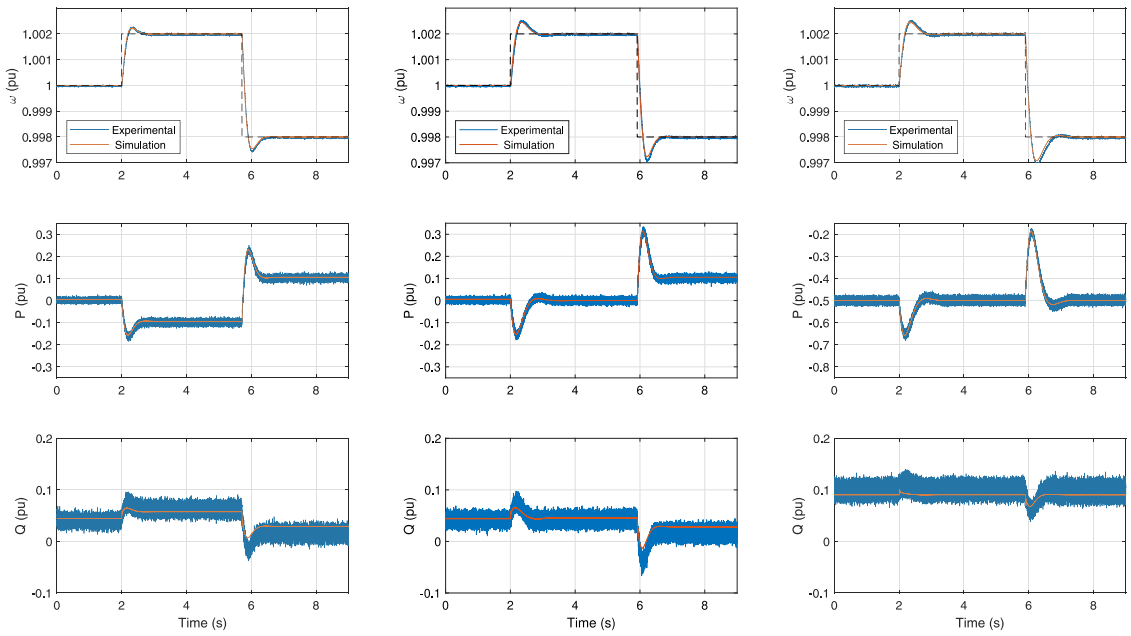

(a) B-GFM mode (b) CL-GFM mode (c) C-GFM mode

Fig. 14. Active and reactive power responses under different operating modes. Grid frequency perturbations of 0.002 and −0.004 pu are applied.

term of the impedance (impedance to resistance ratio of 5). However, the active power is predominant during frequency perturbations, showing a direct relation between both. Experimental results show a higher reactive power exchange, indicating a higher coupling than the obtained in simulation. This discrepancy seems to be related to a higher resistivity in the experimental setup.

4.2.1. B-GFM

Fig. 14(a) shows the operation of the EV charger in B-GFM mode. In this mode, the SoC is inside the operational range and no charging is required, starting with an active power setpoint $P^* = 0$ pu.

The V2G charger provides transient support, in the form of inertia simulation, to both positive and negative grid frequency steps. Due to the dynamic damping term, the active power transient response has a highly damped behaviour, without an excessive overshoot nor ringing.

In B-GFM, as the SoC controller is disabled, the static damping power contribution of the converter is not altered. The charger contributes to support the grid frequency under steady-state conditions. A power exchange of ±0.1 pu is measured for a frequency deviation of ±0.002 pu, corresponding to the D_p term of 50 pu.

4.2.2. CL-GFM

Fig. 14(b) shows the operation of the EV charger in CL-GFM mode. As in B-GFM, the EV is not being charged and the system starts with an active power setpoint of 0 pu.

Under the first over-frequency event, the CL-GFM controller provides support during the transient, but it does not provide steady-state support. This occurs because the integral gain of the SoC controller removes the contribution of the static damping term D_p in approximately 0.8 s, according with the integral gain of 5 rad/s. The active power exchanged during the over-frequency transient is mainly associated to the inertial response of the system, but it is extended for some additional hundred of milliseconds until the static damping power contribution is completely removed by the SoC controller. Once the transient is finished, the active power returns to the pre-event value of 0 pu.

When the under-frequency event occurs, the SoC controller is disabled and the CL-GFM provides both transient and steady-state support. Due to the transition from an over-frequency to an under-frequency condition, the non-linear behaviour of the system can be identified: the CL-GFM supports the grid for a transient of 0.004 pu, but the steady-state support is only given for a deviation of 0.002 pu. This non-linearity leads to a response with a higher overshoot. Once the transient is finished, the steady state active power reaches 0.1 pu, which matches the static damping value.

4.2.3. C-GFM

Fig. 14(c) shows the operation of the EV charger in C-GFM mode. The active power setpoint starts at −0.5 pu, assuming that the vehicle is being charged at half of the charger rated power.

In C-GFM mode, the SoC controller integral action is always enabled, removing the steady-state frequency support and providing only transient support. The response to the over-frequency event is the same as in CL-GFM mode, and the concepts explained in previous subsection are valid. They could be applied to the under-frequency event, where only transient support is also identified. After both under-frequency and over-frequency transients, the active power setpoint returns to the pre-event value of −0.5 pu. One key difference between the C-GFM and the CL-GFM or DL-GFM is that the SoC controller is always enabled, so non-linear behaviour is not present anymore.

Finally, Fig. 15 shows an scope capture of the grid currents and capacitor voltages. The V2G charger, operated in C-GFM mode, is subjected to a 0.004 pu over-frequency. The evolution of the grid currents during the over-frequency event are shown in Fig. 15(a). Analogous to the active power, the amplitude of the grid currents increase during the transient, and they return to the pre-event amplitude due to the SoC controller action.

A zoom from the previous transient is given in Fig. 15(b). The grid currents have a low THD value due to the LCL filter, which removes the high frequency switching components of the inverter. On the other hand, it can be seen that the capacitor voltage and the grid current from the phase A have a phase-shift of 180°, meaning that the charger is consuming mainly active power, with an small reactive power exchange.

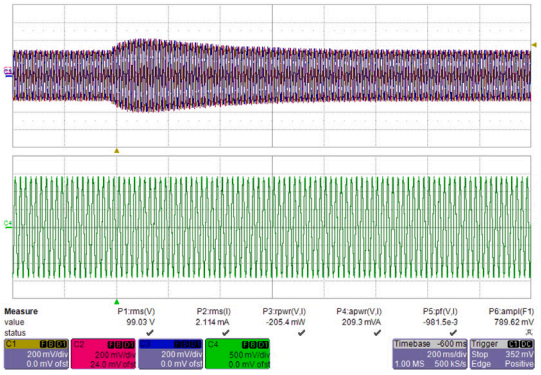

(a) Current transient under a 0.004 pu grid frequency step

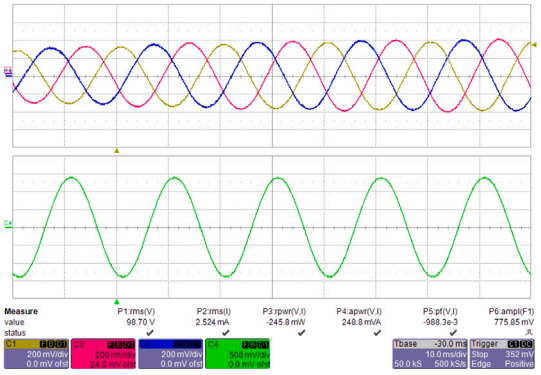

(b) Currents and voltage zoom

Fig. 15. Capacitor voltage (green — phase A) and current (yellow — phase A, pink — phase B, blue — phase C) waveforms during GFM-C operation. Voltage and current scales are 50 V/div and 2 A/div. Time scale is 200 ms/div for (a) and 10 ms/div for (b).

4.3. Effect of SoC controller integral gain

As it was demonstrated in Section 3, the SoC controller will introduce a first order HPF in the static damping power when it is enabled. As the bandwith of the HPF (ω_i) is increased, the closed loop dynamics of the active power will be deteriorated, by reducing the damping of the electromechanical modes. In this context, the dynamic damping term has been suggested as an alternative to keep a proper transient of the system when the SoC controller is enabled.

The proposed analysis has used a bandwith of 5 rad/s for the SoC controller. However, smaller bandwidths could also be used. The main drawback of reducing ω_i is the extra power exchanged during grid frequency perturbations. In this scenario, the contribution of the static damping power will be extended in time, and it will not be limited to inertial response. The transient response will be slightly improved due to the contribution of the static damping term, but the dynamic damping term is still required.

Fig. 16 shows the response of the C-GFM mode for different ω_i values. A grid frequency step of 0.002 pu is applied in all the cases. A ω_i of 5 rad/s will result in a nearly inertial response, whereas an ω_i of 0.1 rad/s extends the static damping power for several seconds, providing higher support at the cost of additional energy injection or absorption.

5. Conclusions

This paper has proposed a modified GFM controller for V2G chargers, which includes an integrated SoC management of the battery. The proposed controller will ensure the voltage source behaviour and the grid support, regardless of the SoC level and the charging requirements

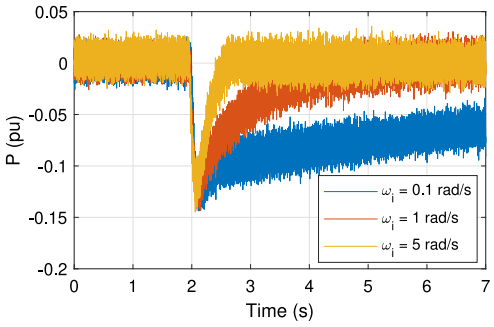

Fig. 16. Active power response in C-GFM using different ω_i values. Response to a grid frequency step of 0.002 pu.

of the EV owner. Moreover, it requires minor modifications to the conventional GFM algorithms.

With the proposed strategy, the V2G charger will always behave as a controlled voltage source that provides inertial response and voltage support to the grid. It will also contribute to primary frequency regulation when the EV does not need charging and the SoC levels are inside operational limits. When the SoC is close to the operational limits, its primary frequency regulation will depend on the perturbation type (over or under-frequency). With this strategy, the EV will keep a partial regulation capability to balance its SoC. Finally, when charging is required, the frequency regulation will be removed to ensure that charging needs are met.

The transfer function and stability analysis of the active power loop have shown that the dynamic damping term of GFM plays a key role in providing a damped transient response, especially as the action of the SoC controller increases. This parameter is tuned to provide a damped power response ($\xi > 0.7$), regardless of the operation mode. Moreover, the transient response of the V2G under frequency excursions can be easily modified through the integral gain of the SoC controller. These transient contributions can go from 1 s for $\omega_i = 5$ rad/s, up to tens of seconds when $\omega_i < 0.1$ rad/s. Smaller integral gains could reduce the dynamic damping term needed, but they will result in additional energy exchange with the grid,

The performance of the controller has been validated through simulation and experimentally, showing that an stable operation is achieved under all the operation modes.

CRediT authorship contribution statement

Ander Ordono: Conceptualization, Formal analysis, Investigation, Software, Validation, Visualization, Writing – original draft. **Francisco Javier Asensio:** Supervision, Writing – review & editing. **Jose Antonio Cortajarena:** Supervision, Validation, Writing – review & editing. **Inmaculada Zamora:** Supervision, Writing – review & editing. **Mikel González-Pérez:** Writing – review & editing. **Gaizka Saldaña:** Writing – review & editing.

Declaration of competing interest

The authors whose names are listed immediately below certify that they have NO affiliations with or involvement in any organization or entity with any financial interest, or non-financial interest in the subject matter or materials discussed in this manuscript.

Data availability

Data will be made available on request.

Acknowledgement

The authors gratefully acknowledge the support from the Basque Government (GISEL Research Group IT1522-22 and ELKARTEK KK-2022/00100), as well as the funding from the European Union-Next Generation EU (INVESTIGO program).

Appendix A. System parameters

See Table A.3.

Table A.3
System parameters.

Base values					
S_b	1 kW	v_b	173 V	f_b	50 Hz
LCL filter					
L_c	0.049 pu	C_f	0.045 pu	L_g	0.0065 pu
R_c	0.006 pu	R_f	0.08 pu	R_g	0.008 pu
Converter general values					
f_{sw}	10 kHz	V_{dc}	1.73 pu		
Current controller					
Bandwidth	500 Hz	k_{pc}	0.49	k_{ic}	18.9
Virtual admittance					
L_v	0.3 pu	R_v	0.06 pu		
Active power loop					
D_p	50 pu	H	4 s	D_d	0.08 pu
τ_d	0.008 s				
SoC controller					
ω_i	5 rad/s				
Reactive power control					
m_q	0.1 pu	τ_q	20 ms	Q^*	0 pu
v^*	1 pu				
Grid					
v_g	1 pu	Z_G	0 pu	f_g	1 pu

References

[1] Shaukat N, Islam MR, Rahman MM, Khan B, Ullah B, Ali SM, et al. Decentralized, democratized, and decarbonized future electric power distribution grids: A survey on the paradigm shift from the conventional power system to micro grid structures. IEEE Access 2023;11:60957–87. http://dx.doi.org/10.1109/ACCESS.2023.3284031.

[2] Dreidy M, Mokhlis H, Mekhilef S. Inertia response and frequency control techniques for renewable energy sources: A review. Renew Sustain Energy Rev 2017;69:144–55. http://dx.doi.org/10.1016/j.rser.2016.11.170.

[3] Jayasinghe G, Bahrani B. Stability-enhancing measures for weak grids study milestone 2 Report. Tech. rep., Monash University; 2021.

[4] Parmar KS, Majhi S, Kothari D. Load frequency control of a realistic power system with multi-source power generation. Int J Electr Power Energy Syst 2012;42(1):426–33. http://dx.doi.org/10.1016/j.ijepes.2012.04.040.

[5] Gomis-Bellmunt O, Tavakoli SD, Lacerda VA, Prieto-Araujo E. Grid-forming loads: Can the loads be in charge of forming the grid in modern power systems? IEEE Trans Smart Grid 2023;14(2):1042–55. http://dx.doi.org/10.1109/TSG.2022.3202646.

[6] Sovacool BK, Kester J, Noel L, Zarazua de Rubens G. Actors, business models, and innovation activity systems for vehicle-to-grid (V2G) technology: A comprehensive review. Renew Sustain Energy Rev 2020;131:109963. http://dx.doi.org/10.1016/j.rser.2020.109963.

[7] ur Rehman U. A robust vehicle to grid aggregation framework for electric vehicles charging cost minimization and for smart grid regulation. Int J Electr Power Energy Syst 2022;140:108090. http://dx.doi.org/10.1016/j.ijepes.2022.108090.

[8] Sevdari K. Ancillary services and electric vehicles: An overview from charging clusters and chargers technology perspectives. Renew Sustain Energy Rev 2022.

[9] Khokhar B, Dahiya S, Parmar KPS. Load frequency control of a multi-microgrid system incorporating electric vehicles. Electr Power Compon Syst 2021;49(9–10):867–83. http://dx.doi.org/10.1080/15325008.2022.2049648.

[10] Khokhar B, Parmar KPS. A novel adaptive intelligent MPC scheme for frequency stabilization of a microgrid considering SoC control of EVs. Appl Energy 2022;309:118423. http://dx.doi.org/10.1016/j.apenergy.2021.118423.

[11] Khokhar B, Parmar KS. A novel intelligent distributed model predictive control scheme for load frequency control of a multimicrogrid system incorporating electric vehicles. In: Advanced frequency regulation strategies in renewable-dominated power systems. Elsevier; 2024, p. 345–66. http://dx.doi.org/10.1016/B978-0-323-95054-1.00006-8.

[12] Khokhar B, Dahiya S, Singh Parmar KP. A robust cascade controller for load frequency control of a standalone microgrid incorporating electric vehicles. Electr Power Compon Syst 2020;48(6–7):711–26. http://dx.doi.org/10.1080/15325008.2020.1797936.

[13] Rosso R, Wang X, Liserre M, Lu X, Engelken S. Grid-forming converters: Control approaches, grid-synchronization, and future trends—A review. IEEE Open J Ind Appl 2021;2:93–109. http://dx.doi.org/10.1109/OJIA.2021.3074028.

[14] Muhssin MT, Obaid ZA, Al-Anbarri K, Cipcigan LM, Ajaweed MN. Local dynamic frequency response using domestic electric vehicles. Int J Electr Power Energy Syst 2021;130:106920. http://dx.doi.org/10.1016/j.ijepes.2021.106920.

[15] Woong Shim J, Verbic G, Hur K. Grid-supportive electric vehicle charging methodology with energy management for coordinated frequency control. IET Gener, Transm Distribution 2021;15(24):3474–8. http://dx.doi.org/10.1049/gtd2.12267.

[16] Scarabaggio P, Carli R, Cavone G, Dotoli M. Smart control strategies for primary frequency regulation through electric vehicles: A battery degradation perspective. Energies 2020;13(17):4586.

[17] Sanchez F, Gonzalez-Longatt F, Bogdanov D. Impact assessment of frequency support by electric vehicles: Great britain scenario 2025. In: 2018 20th international symposium on electrical apparatus and technologies (SIELA). 2018, p. 1–4. http://dx.doi.org/10.1109/SIELA.2018.8447085.

[18] Meng J, Mu Y, Jia H, Wu J, Yu X, Qu B. Dynamic frequency response from electric vehicles considering travelling behavior in the Great Britain power system. Appl Energy 2016;162:966–79. http://dx.doi.org/10.1016/j.apenergy.2015.10.159.

[19] Jan MU, Xin A, Rehman HU, Abdelbaky MA, Iqbal S, Aurangzeb M. Frequency regulation of an isolated microgrid with electric vehicles and energy storage system integration using adaptive and model predictive controllers. IEEE Access 2021;9:14958–70. http://dx.doi.org/10.1109/ACCESS.2021.3052797.

[20] Rezkalla M, Zecchino A, Martinenas S, Prostejovsky AM, Marinelli M. Comparison between synthetic inertia and fast frequency containment control based on single phase EVs in a microgrid. Appl Energy 2018;210:764–75.

[21] Fakhari Moghaddam Arani M, Mohamed YA-RI. Cooperative control of wind power generator and electric vehicles for microgrid primary frequency regulation. IEEE Trans Smart Grid 2018;9(6):5677–86. http://dx.doi.org/10.1109/TSG.2017.2693992.

[22] Hernández J, Sanchez-Sutil F, Vidal P, Rus-Casas C. Primary frequency control and dynamic grid support for vehicle-to-grid in transmission systems. Int J Electr Power Energy Syst 2018;100:152–66. http://dx.doi.org/10.1016/j.ijepes.2018.02.019.

[23] Song G, Cao B, Chang L. Review of grid-forming inverters in support of power system operation. Chin J Electr Eng 2022;8(1):1–15. http://dx.doi.org/10.23919/CJEE.2022.000001.

[24] Zhao X, Thakurta PG, Flynn D. Grid-forming requirements based on stability assessment for 100% converter-based Irish power system. IET Renew Power Gener 2022;16(3):447–58. http://dx.doi.org/10.1049/rpg2.12340.

[25] Dai Y, Zhang L, Chen Q, Zhou K, Hua T. Multi-VSG-based frequency regulation for uninterruptible power AC micro-grid with distributed electric vehicles. Int J Electr Power Energy Syst 2022;137:107785. http://dx.doi.org/10.1016/j.ijepes.2021.107785.

[26] Suul JA, DArco S, Guidi G. Virtual synchronous machine-based control of a single-phase bi-directional battery charger for providing vehicle-to-grid services. IEEE Trans Ind Appl 2016;52(4):3234–44. http://dx.doi.org/10.1109/TIA.2016.2550588.

[27] Sal y Rosas D, Zarate A. Single-phase grid-forming strategy with power decoupling implementation for electrolytic-capacitor-free EV smart battery charger. Energies 2023;16(2). http://dx.doi.org/10.3390/en16020894.

[28] Laba Y, Bruyère A, Colas F, Guillaud X, Silvestre B. Operating grid-forming control on automotive reversible battery charger. In: 2021 IEEE vehicle power and propulsion conference. VPPC, 2021, p. 1–6. http://dx.doi.org/10.1109/VPPC53923.2021.9699305.

[29] Li P, Hu W, Xu X, Huang Q, Liu Z, Chen Z. A frequency control strategy of electric vehicles in microgrid using virtual synchronous generator control. Energy 2019;189:116389. http://dx.doi.org/10.1016/j.energy.2019.116389.

[30] Deng H, Fang J. State-space modeling, stability analysis, and controller design of grid-forming converters with distributed virtual inertia. Front Energy Res 2022;10:833387. http://dx.doi.org/10.3389/fenrg.2022.833387.

[31] Dolado J, Rodríguez Amenedo JL, Arnaltes S, Eloy-Garcia J. Improving the inertial response of a grid-forming voltage source converter. Electronics 2022;11(15):2303. http://dx.doi.org/10.3390/electronics11152303.

[32] Ruan X, Wang X, Pan D, Yang D, Li W, Bao C. Control techniques for LCL-type grid-connected inverters. CPSS power electronics series, Singapore: Springer Singapore; 2018, http://dx.doi.org/10.1007/978-981-10-4277-5.

[33] Rathnayake DB, Akrami M, Phurailatpam C, Me SP, Hadavi S, Jayasinghe G, et al. Grid forming inverter modeling, control, and applications. IEEE Access 2021;9:114781–807. http://dx.doi.org/10.1109/ACCESS.2021.3104617.

[34] Lai NB, Baltas GN, Rodriguez P. Multi-rotor virtual machine for grid-forming converter to damp sub-synchronous resonances. IEEE Access 2021;9:128178–87. http://dx.doi.org/10.1109/ACCESS.2021.3112070.

[35] Chen J, O'Donnell T. Analysis of virtual synchronous generator control and its response based on transfer functions. IET Power Electron 2019;12(11):2965–77. http://dx.doi.org/10.1049/iet-pel.2018.5711.

[36] Rodriguez-Amenedo JL, Gomez SA. Damping low-frequency oscillations in power systems using grid-forming converters. IEEE Access 2021;9:158984–97. http://dx.doi.org/10.1109/ACCESS.2021.3130333.

[37] Vidal Leon JD, Tarraso A, Candela JI, Rocabert J, Rodriguez P. Grid-forming controller based on virtual admittance for power converters working in weak grids. IEEE J Emerg Selected Top Ind Electron 2023;1–11. http://dx.doi.org/10.1109/JESTIE.2023.3244744.

[38] Yang D, Wu H, Wang X, Blaabjerg F. Suppression of synchronous resonance for VSGs. J Eng 2017;2017(13):2574–9. http://dx.doi.org/10.1049/joe.2017.0792.

[39] Aragon D, Unamuno E, Ceballos S, Barrena J. Comparative small-signal evaluation of advanced grid-forming control techniques. Electr Power Syst Res 2022;211:108154. http://dx.doi.org/10.1016/j.epsr.2022.108154.

[40] Zhang W, Cantarellas AM, Rocabert J, Luna A, Rodriguez P. Synchronous power controller with flexible droop characteristics for renewable power generation systems. IEEE Trans Sustain Energy 2016;7(4):1572–82. http://dx.doi.org/10.1109/TSTE.2016.2565059, URL http://ieeexplore.ieee.org/document/7470277/.

[41] Deng H, Fang J, Qi Y, Tang Y, Debusschere V. A generic voltage control for grid-forming converters with improved power loop dynamics. IEEE Trans Ind Electron 2023;70(4):3933–43. http://dx.doi.org/10.1109/TIE.2022.3176308.